Boundary effects in finite size plasmonic crystals: focusing and routing telecom plasmonic beams

M. I. Benetou[1=], J.-S. Bouillard[2*=], P. Segovia-Olivera[2=],
W. Dickson[2], B.C. Thomsen[1], P. Bayvel[1] and A.V. Zayats[2]

[1] Optical Networks Group, Department of Electronic and Electrical Engineering, University College London, London WC1E 7JE, United Kingdom
[2] Nano-optics and Near-field Spectroscopy Group, Department of Physics, King's College London, Strand, LondonWC2R 2LS, United Kingdom
[=] Equal contributions
*Current address: Department of Physics and Mathematics, University of Hull, Cottingham Road, Hull HU6 7RX, United Kingdom

Abstract: Plasmonic crystals, which consist of periodic arrangements of surface features at a metal-dielectric interface, allow the manipulation of optical information in the form of surface plasmon polaritons. Here we investigate the excitation and propagation of plasmonic beams in and around finite size plasmonic crystals at telecom wavelengths, highlighting the effects of the crystal boundary shape and illumination conditions. Significant differences in broad plasmonic beam generation by crystals of different shapes are demonstrated, while for narrow beams, the propagation onto the smooth metal film is less sensitive to the crystal boundary shape. We show that by controlling the boundary shape, the size and the excitation beam parameters, directional control of propagating plasmonic modes and associated beam parameters such as angular beam splitting, focusing power and beam width can be efficiently achieved. This provides a promising route for robust and alignment-independent integration of plasmonic crystals with optical communication components.

1. Introduction

The integration of various photonic functionalities, along with the reduction in size and energy consumption of integrated photonic systems and telecom components, is essential for the future developments of information processing and transmission. Plasmonic technology, providing sub-wavelength electromagnetic field confinement and strong field enhancement due to the coupling of photons with collective electron oscillations at a metal-dielectric interface, offers unprecedented opportunities in the design of sub-wavelength waveguide circuitry and miniaturised photonic devices operating with low-power control signals [1-3]. An increasing toolbox of plasmonic components is constantly being developed, with a variety of plasmonic and hybrid plasmonic / photonic waveguides and waveguide components. Key devices based on plasmonic technology such as ring- and disk- waveguide resonators, Mach-Zehnder interferometers, Bragg-gratings and nonlinear components have been demonstrated for integrated nanophotonic applications [4-14]. However, the vast majority of on-chip optical applications requires interfacing with optical fibre technology, used ubiquitously for optical

communication. In silicon-based photonic applications, alternate geometries have been explored to ensure mode matching between the optical fibre and the nanophotonic waveguide, and thus improve on the simple inefficient "butt-coupling". Such techniques include the use of complex 3D tapers [15] or inverse tapers [16-18], and multigrating coupler arrangements [19]. Nevertheless, all those techniques rely on in-plane end-fire coupling, therefore necessitating time consuming and expensive polishing or controlled cleaving since they have to be located at the edge of the optical chip.

Another family of couplers uses 1D diffractive structures, in conjunction with a taper, in order to match the grating diffraction orders and the waveguide modes [20]. While this technique allows for direct coupling of out-of-plane incident light to photonic waveguided modes, it imposes restrictions on both the manufacturing process and large scale applications. In order to address those issues, dielectric and plasmonic chirped diffraction gratings and plasmonic particles have been proposed [21-24]. Despite the high component density offered by plasmonic systems [4, 5, 25], the integration of plasmonic functionalities with optical fibre interconnects has been much less investigated.

Periodically nanostructured metal films, which allow for the efficient coupling of incoming optical signal into surface plasmon polariton (SPP) waves [3], offer a promising route to interface plasmonic devices with conventional telecommunication systems. Such plasmonic structures, commonly referred to as surface plasmon polaritonic crystals (SPPCs) or simply plasmonic crystals [3], provide an opportunity to excite and manipulate plasmonic beams with wavelength [13, 26-29] and polarisation [29-31] control. Both active and passive functionalities of SPPCs have been extensively studied for applications in diverse areas, ranging from enhanced sensing [32, 33] to advanced optoelectronic devices [34-36]. Active functionality relies on the strong sensitivity of the SPP Bloch modes supported by the SPPC to the refractive index of either the dielectric, which can be controlled with applied electric or magnetic field, all-optically or acoustically [11, 37-40], or the metal film which can be thermally adjusted [41]. Passive applications rely on the wavelength and polarisation dispersion of SPP Bloch modes, as well as on the SPPC ability to couple these modes onto the smooth film. The signals conditioned by the SPPC can then be coupled back into optical links or integrated photodetectors. A wide variety of passive telecom nanophotonic devices based on plasmonic crystal properties have been proposed, including 4-level polarisation discriminators, polarimeters, ultrahigh-resolution wavelength demultiplexers, and broadband couplers to photonic or plasmonic waveguides [14, 28, 30, 34, 42, 43].

To date, the understanding of the optical properties of SPPC has been achieved largely by considering infinite crystal lattices, with the role of the boundary shape being largely overlooked, despite its importance for applications in finite size plasmonic structures. Appropriate design of the boundary shape allows for the shaping of SPP beams coupled to the smooth metal film by controlling their refraction and their relative phase relations at the crystal boundary, which can be used for key telecommunication applications such as information demultiplexing or optimisation of device parameters, such as operation bandwidth and crosstalk.

In this paper, the effects of the finite size SPPC boundary shape and the illumination parameters on the excitation of plasmonic beams under collimated and focussed illumination were studied at the telecom relevant wavelengths around 1550 nm. In this spectral range, the boundary effects and their applications can be highlighted which are difficult to realize in the visible spectral range due to a shorter SPP propagation distance [42]. Scanning near-field optical microscopy (SNOM) was used to experimentally visualise the near-field intensity distributions of plasmonic modes on and around the nanostructured metal films, and a numerical model based on the point-dipole approximation was developed to compare with the experimental results and explore the vast parameter space. By engineering the SPPC boundary shape and varying the illumination parameters, control over the properties of the SPP beams excited by the structure can be achieved. Manipulation of the SPP beams lateral extension and

propagation direction, in-plane focusing, SPP beam-splitting, refraction and wavelength-dependent SPP coupling are also demonstrated, opening the way for numerous on-chip applications.

2. Samples and Experiment

The SPPCs under investigation were fabricated using focussed ion beam (FIB) milling in a 50 nm thick gold film deposited onto a glass substrate using magnetron sputtering. The plasmonic crystals consisted of circular holes of 300 nm diameter periodically arranged in a square lattice with a 1530 nm period, optimised to excite SPPs at the telecom wavelength of 1550 nm. In order to investigate the effects of the SPPC boundary shape, both square and circular boundaries were considered, with 40 μm width and 40 μm diameter, respectively (Fig. 1(c,d)).

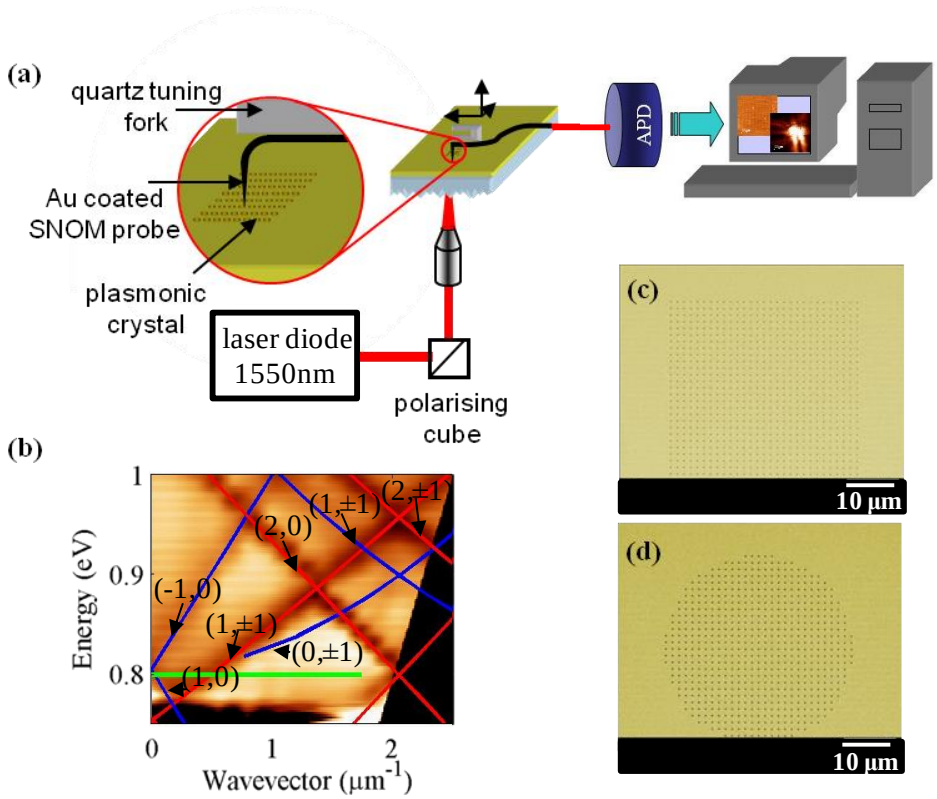

Fig. 1: (a) SNOM experimental arrangement. (b) Dispersion of the SPP modes on the crystal. The green line indicates the spectral range of wavevectors excited under the illumination with a 1550 nm focussed laser beam (N.A.=0.43). Blue and red lines represent the SPP Bloch mode positions calculated in the empty lattice model for Au-air and Au-glass interfaces, respectively. (c), (d) Scanning electron microscope (SEM) images of the square and circular SPPCs, respectively.

The SPP band diagram of the plasmonic crystals (Fig. 1(b)) representing the SPP Bloch modes supported by the lattice, was reconstructed from the measured zeroth-order far-field transmission spectra of the nanostructures under p-polarised collimated illumination and simulated using the empty lattice model [3, 37]. For the crystal size used in this work, the far-field transmission dispersion is independent of the crystal boundary shape and is essentially governed by the lattice parameters.

The propagation of the SPP Bloch modes within the crystal, and their refraction at the boundary with the smooth metal film, were investigated by directly imaging them with SNOM [44]. A laser diode, emitting at a wavelength of 1550 nm, was used to illuminate the SPPCs in transmission. The beam was expanded, collimated and polarised in the case of a collimated illumination, and a microscope objective with a numerical aperture (N.A.) of 0.43 was used in the case of a focussed illumination. The SNOM probe was a pulled and subsequently gold-coated 9.3 μm core standard single-mode optical fibre at the end of which a nano-aperture was created using FIB. The tapered end of the fibre was bent at 90° and mounted on a quartz tuning fork [44, 45] operating in tapping mode. The light collected locally by the interaction of the SNOM probe with the near-field at the surface of the sample was then detected by an avalanche photodiode.

3. Numerical Model

The optical properties of SPPCs were simulated using the vectorial model for multiple SPP scattering in which surface scatterers are considered as emitting point-like dipoles [46-48]. This assumption makes it possible to construct a Green´s tensor describing the SPP scattering by such dipoles. The validity of the model has been established for relatively large inter-particle distances (>$\lambda/2$) relevant for SPPC simulations, whereas for smaller distances multipolar contributions have to be included in the scattered field [48, 49]. Within this model, the polarisation of the ith-scatterer in the SPP crystal takes the form:

$$\vec{P}_i = \underline{a} \cdot \vec{E}_0\left(\vec{r}_i\right) + k_0^2 \sum_{j=1, j\neq i}^{N} \underline{a} \cdot \underline{G}\left(\vec{r}_i, \vec{r}_j\right) \cdot \vec{P}_j \qquad (1)$$

where $\underline{a}$ is the polarisability tensor of the scatterer [50], $\vec{E}_0\left(r_i\right)$ is the incident field at the site of scatterer i, $k_0=2\pi/\lambda$ is the wave vector of the incoming field in the free space, and $\underline{G}\left(\vec{r}_i, \vec{r}_j\right)$ is the Green tensor for SPP to SPP scattering (sometimes called the total field propagator) [48, 49].

The Green tensor is the sum of a direct contribution $\underline{G}^d$, in this case the free space Green´s tensor, and an indirect contribution, $\underline{G}^S$, that describes both the reflection from the metal-dielectric interface and the excitation of SPPs. Since the SPP effects are dominant over the reflections from the metal-dielectric interface, the Green's function tensor can be approximated by [50] .

$$\underline{G}_{SPP}(\vec{r},\vec{r}\,') \approx -i\frac{k_{SPP}}{2}\frac{e^{-\sqrt{\varepsilon_d/(-\varepsilon_m)}k_{spp}(z+h)}}{\sqrt{\varepsilon_d/(-\varepsilon_m)}\left(1-\frac{\varepsilon_d^2}{\varepsilon_m^2}\right)\frac{\varepsilon_d+\varepsilon_m}{\varepsilon_d\varepsilon_m}}H_0^{(1)}(k_{spp}p)\left(\hat{z}\hat{z}-\frac{\varepsilon_d}{\varepsilon_m}\hat{p}\hat{p}+(\hat{z}\hat{p}-\hat{p}\hat{z})i\sqrt{\frac{\varepsilon_d}{-\varepsilon_m}}\right) \quad (2)$$

where $k_{SPP}=k_0\sqrt{\frac{\varepsilon_m\varepsilon_d}{\varepsilon_m+\varepsilon_d}}$ is the SPP wavevector, ε_m and ε_d are the dielectric constants of the metal and dielectric, respectively, H_0^1 is the zero-order Hankel function of the first kind, *p* is the projection of the scatterer-(observation point) distance on the metal-dielectric interface, and *z* and *h* are the height of the observation point and the source point, respectively [50]. The self-consistent field around the scatterer is then determined as

$$\vec{E}(\vec{\mathrm{r}})=\vec{E}_0(\vec{\mathrm{r}})+k_0^2\sum_{i=1}^{N}\underline{G}(\vec{r},\vec{r}_i)\cdot\vec{P}_i \quad (4)$$

The excitation and propagation of SPPs on the SPPCs were simulated under the two different illumination conditions considered in this work: (i) *x*-polarised, collimated illumination described by $\vec{E}=E_0\hat{x}$ or (ii) *x*-polarised, focussed Gaussian beam illumination for which the illuminating field structure is described in Ref. [51].

4. Results and Discussions

4.1. Collimated illumination

The effects of the SPPC boundary shape on the coupling to SPPs on the smooth metal film were first investigated under linear-polarised plane wave illumination at normal incidence. Figure 2 shows the experimental and calculated near-field intensity distributions on and around the nanostructured area under such illumination conditions. The excitation of the counter-propagating (±1, 0) SPP Bloch modes, leading to the formation of the well-known standing wave pattern on the nanostructured area [24, 44, 45] and the SPP beams on the smooth metal film after refraction at the crystals' boundary can be clearly observed. The higher SPP intensity in the lower half of the structures observed in the experimental images (Fig. 2(a,d)) is due to a small deviation from perfect normal incidence illumination conditions (a deviation of 1º is enough to result in preferential coupling to the one of the (±1, 0) modes as seen in Fig. 1b). As a result, SPP modes travelling in the negative *x* direction were preferentially excited, resulting in an increased near-field intensity at the corresponding boundary. This does not however modify the eigenmodes of the crystal and the SPPs propagating on the nanostructured area are the well-defined (±1, 0) SPP Bloch modes. Consequently, their refraction at the boundary of the crystal and their propagation onto the smooth metal film is not affected. Furthermore, it is worth noting that the excitation of SPPs onto the smooth metal film arising from the in-plane scattering of individual holes on the crystal boundary can be neglected as this is a non-resonant process, with a scattering efficiency 2 orders of magnitude lower than the collective excitation probed in this work.

The SPPC boundary acts as an interface where SPPs are either reflected back into the crystal or transmitted onto the smooth metal film after refraction. As a direct consequence of the finite size of the structures, focusing of the SPPs coupled onto the smooth metal film can be observed both experimentally and numerically (Fig. 2). This focusing effect, illustrated by

a reduction of the SPP beam waist with increasing distance from the crystal boundary, is the result of the interference between SPPs coupled onto the smooth metal film from different parts of the SPPC boundary, each with a different phase relation in a given propagation direction, defined by the boundary shape. Assuming *N* scatterers contributing to the field at a point *P* on a smooth metal film, the effect can approximately be predicted analytically, describing the resulting electric field [52]: $E_P \sim \sum_{i=1}^{N} E_i(\vec{r}_i)/r_i^{1/2} e^{-i\vec{k}_{SPP}\vec{r}_i}$, where E_i is the electric field amplitudes at the i^{th} scatterer, $\vec{r}_i$ is the co-ordinate of the i^{th} scatterer with respect to the observation point *P*, and $\vec{k}_{SPP}$ is the SPP wavevector. Thus, the phase differences $\Delta\varphi_{ij} = \vec{k}_{SPP}|\vec{r}_i - \vec{r}_j|$ determine the interference process depending on the position of the scatterers at the boundary of one or another shape. If only several neighbouring scatterers at the boundary are involved, the phase changes are not significant enough to modify strongly the field distribution for different boundary shapes.

The numerically calculated beam profiles for the square and circular structures at several distances from the SPPC centre, along with the experimental SPP profile, measured at a distance of 45 μm from the crystal centre, are plotted in Fig. 3. Whilst there are small differences between the experiment and model, the profile shape and its dependence on the boundary geometry is clearly recovered with modelling. The focusing effect is highlighted further in Fig. 3(c) which depicts the experimentally measured and numerically calculated full-width half maximum (FWHM) of the SPP beam as defined in Fig. 3(a) for both the square and the circular SPPCs as a function of distance from the crystal centre. The width of the outcoupled SPP beam is smaller in the case of the circular boundary compared to the square boundary, but for both structures, the SPP beam width decreases as it propagates away from the structure.

In order to compare the focusing properties of the two different boundary shapes in the context of on-chip signal processing, Fig. 3(d) shows the aperture size needed to collect 50% of the total SPP power as a function of the distance from the SPPC centre. It can be seen that a circular boundary exhibits a stronger effective in-plane focusing power, with a focal length of 350 μm and a 'depth of focus' (DOF) of 75 μm, compared to 450 μm and 110 μm, respectively, for a square boundary. Here, the DOF is defined as the area over which the size of the detector required to detect 50% of the SPP power varies by less than 1% from its minimum value at the focal point. Interestingly, due to the complex beam profiles, defocusing of the SPP beam in both cases takes place at the same rate.

The differences observed in the focussing of SPPs depending on the SPPC shape illustrate the necessity for adequate boundary engineering, such as varying the nanostructure shape and size which offers additional control over the generated plasmonic beams and provides opportunities for generating complex plasmonic beam shapes [42, 53-58].

In addition to the focusing aspect, multiple bottle-type SPP beams can be observed for both boundary shapes considered here, further illustrating the possible control over the phase of individual SPP beams coupled onto the smooth metal films. Such phase-controlled plasmonic beam formation was recently used for the generation of cosine-Gaussian and other non-diffracting SPP beams [54-56]. However, whilst for the generation of such complex-beam-profiles and non-diffracting SPP beams specially designed geometries are used to provide the required phase relations, the work presented here illustrates that careful engineering of the plasmonic crystals boundary can also be used for this purpose.

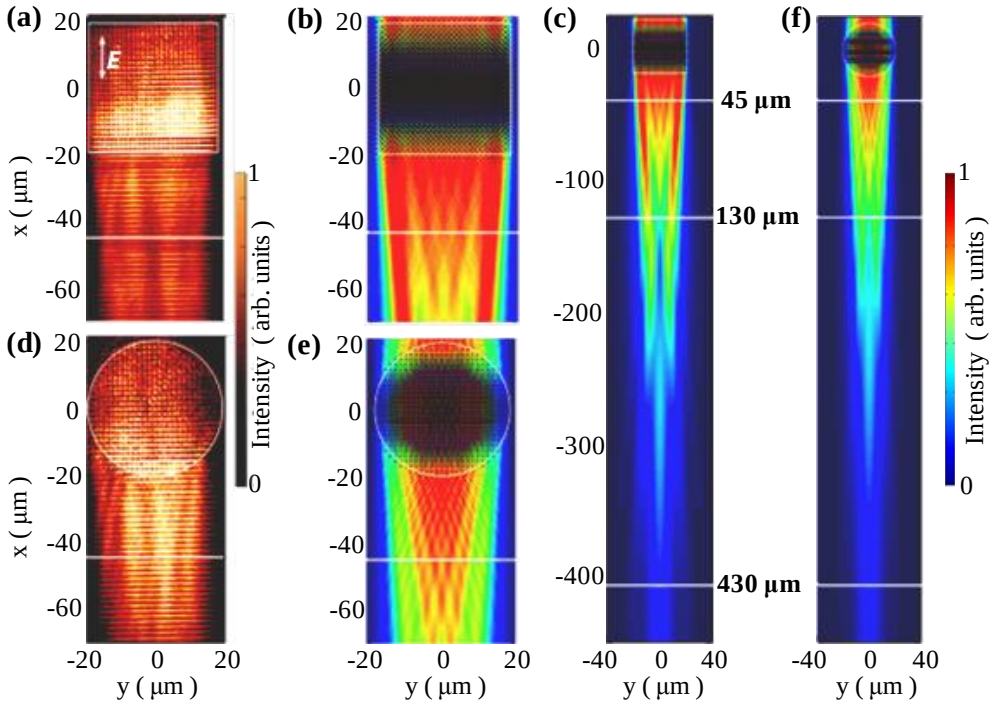

Fig. 2. (a,d) Experimentally measured and (b-c, e-f) numerically simulated SPP intensity distributions on and near the square lattice SPPCs with 1530 nm period for (a-c) square (40 µm width) and (d-f) circular (40 µm diameter) boundaries. Collimated illumination wavelength is 1550 nm; polarisation is indicated in (a). White lines indicate the position of the cross-sections of the intensity distributions plotted in Fig. 3.

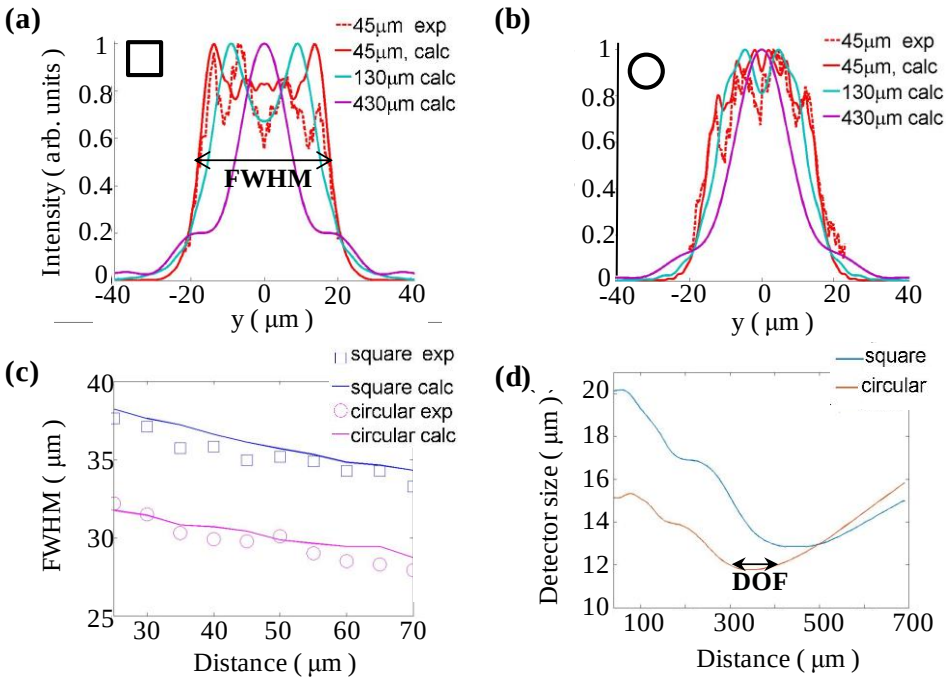

Fig. 3. (a), (b) Cross-sections of the SPP beams radiated by the square (a) and circular (b) SPPCs at several distances from the SPPC centre. Positions of the cross-sections are indicated with white lines in Fig. 2. (c) FWHM of the experimentally measured and numerically calculated SPP profiles as a function of distance from the SPPC centre. (d) The distance dependence of the minimum aperture size needed to detect 50% of the total SPP power (recalculated from the field distributions in Fig. 2).

4.2. Focussed illumination

To increase control over the generated SPP waves and further explore the effects of the crystal boundary shape, focussed illumination of a part of the SPPCs was studied. Such an illumination provides a localised source of SPP waves inside the crystal. SPP beams are excited and subsequently couple to the eigenmodes of the SPPC, dictated by the plasmonic band diagram of the structure [42]. This illumination scheme allows for the direct visualisation of the SPP beams propagating inside the nanostructured area followed by their refraction at the crystal boundary and coupling to smooth film SPP modes; as a result of the local illumination, 10 μm in diameter, and the subsequent filtering by the lattice, only the SPPs coupled to the crystal eigenmodes are incident onto the boundary [42]. Additionally, the SPP modes excited within the crystal on the Au-glass interface are also visible on the Au-air interface, as they couple via the holes forming the crystal, which further increases the complexity of the near-field distribution over the nanostructured area.

In order to differentiate between the effects resulting from the reduced illumination spot size and from the larger incident wavevector spectrum provided by the focussed illumination, one can consider a gedanken experiment with a narrow-beam collimated illumination with the spot size identical to the focussed case (10 μm diameter). Despite being Fourier invalid, this artificial notion allows to probe the effects linked to the reduced illumination spot size

independently of the mixing of the incident wavevectors. Using this artificial illumination scheme, the SPP distribution on the surface and in the vicinity of the SPPCs (square and circular) was simulated for the Au-air interface (Fig. 4(a,b)), for the Au-glass interface (Fig. 4(c,d)) and as probed using the SNOM experimental arrangement (Fig. 4(e,f)), considering a coupling coefficient of 0.1 between the SPP modes on the Au-glass and Au-air interfaces within the crystal (for the wavelength considered here, the SPP fields do not penetrate the metal film to a sufficient depth to lead to interference between the SPPs propagating at different interfaces, so that incoherent summation only at the position of holes is used to simulate the effect). In general, the spectrum of the populated SPP Bloch modes is defined by the overlap, in both the frequency space and the momentum space, of the in-plane scattering diagram of the illuminated scatterers and the SPP Bloch modes sustained by the nanostructured area defined by the plasmonic band-diagram of the crystal [37]. As a result, it can be seen that, independently of the illumination beam size, in the case of a collimated illumination, the same SPP Bloch mode spectrum is observed on the Au-air interface (Figs 2(b,e) and 4(a,b)). The size of the illumination spot however determines the number of elements of the crystal contributing to the generation of SPPs, directly influencing the width of the generated SPP beams. This "antenna-type" effect also leads to the non-resonant excitation of the (1,±1) Au-glass SPP modes due to the light scattering into non-resonant SPPs, followed by filtering by the crystal lattice [42]. For a reduced illumination spot size, the narrow width of the generated SPP beams results in an interaction with a smaller number of scatterers at the crystal boundary, so that the phase-differences from the scatterers contributing to the SPP beam formation on the smooth film are negligible, resulting in near conventional, diffraction governed, SPP beam propagation, different from the complex SPP beams generated with a larger number of scatterers observed in Fig. 2.

In addition to a reduced illumination spot size, the wide range of incident wavevectors present in the focussed illumination (Fig. 1(b)) results in the simultaneous excitation of a number of SPP Bloch modes propagating in different directions (Fig. 5 and 6). The complex angular distribution of the SPP beams generated for an off-centre illumination at a wavelength of 1550 nm as experimentally measured and numerically calculated is presented in Fig. 5. Similarly to the reduced size plane wave above, in order to analyse the complex angular distribution of the SPP beams detected at the SNOM images (Fig. 5(a,b)) the SPP intensity distributions were simulated independently for each interface and then combined, using the same coupling coefficient of 0.1 within the crystal, for comparison with the experimental near-field distributions. It can be observed that the combined calculated near-field distributions reproduce the full range of SPP beams observed experimentally ((Fig. 5(a,b)). The (±1,0) and the (0,±1) eigenmodes, propagating in the x and y directions, respectively, are clearly visible on the Au-air interface. Additionally, due to the coupling through the apertures waveguided modes in the SPPC, the (1,±1) eigenmodes corresponding to the Au-glass interface, propagating at ±45^o to the x and y axes, are observed within the crystal on the Au-air interface. The relative coupling efficiency to each SPP eigenmode is directly related to the wavevector spectrum and the polarisation states present in the illumination spot [30, 37, 42], controlled by the illumination conditions. The corresponding SPP intensity distributions in the case of the central illumination are plotted in Fig. 6(a,b). It can be observed that displacing the illumination spot away from the SPPC geometrical centre has no effect on the spectrum of the excited SPP Bloch modes, governed by the illumination spot and the symmetry of the lattice. Comparison of the field distributions for the square and circular SPPCs shows much smaller differences than for the collimated illumination of the entire crystal (Figs. 2, 5 and 6). This is, as discussed above, a direct consequence of the reduced lateral width of the SPP beams excited under the focussed illumination conditions.

Fig. 6(c-d) shows the SPP intensity at several radii around the SPPC centre, inside (3 μm and 18 μm) and outside (29 μm) the SPPC, for the case of a centred illumination. As expected, the (±1, 0) Bloch modes on the Au-air interface are excited with a higher efficiency due to the

orientation of incident light polarisation. Additionally, two SPP beams propagate on the crystal in both the (±1, 0) and (0, ±1) directions, at angles 61^{o} and 119^{o}, and 150^{o} and 210^{o} to the *y*-axis respectively; their angular beam separation on the surrounding smooth film can be manipulated by engineering the local boundary curvature at the points where these refract onto the smooth film, which can be useful for micro-beam splitting applications. This SPP splitting, along with the relative intensity of the various populated Bloch modes, is a direct result of the complex in-plane scattering cross-section of the illuminated scatterers in the lattice [42, 59]. In the case of a centred illumination, the coupling efficiency in the two counter-propagating eigenmodes is the same, while small variations are observed for the off-centre illumination (Figs. 5(g-h) and 6(a-b)). Experimentally, the refraction is clearly observed in Fig. 5(a,b), and is more pronounced for SPP beams impinging on the boundary at larger angles. This opens a potential route for wavelength demultiplexing as, at this interface, SPP beams of different wavelengths will be refracted at different angles. In the simulations, the refraction is underestimated as the model uses dipoles positioned on smooth metal film to simulate the grating. As a result, the difference in effective index between the nanostructured area and the smooth metal film is not as large as in the experimental case where the apertures are filled with air.

Furthermore, due to coupling of the SPP Bloch modes to the holes of the nanostructure, SPP Bloch modes propagating on the Au-glass interface contribute to the complex excitation of plasmonic beams on the Au-air interface within the crystal. After being coupled through the nanoapertures forming the crystal, the (1, ±1) modes preferentially excited on the Au-glass interface (Fig. 5(e,f)), cannot propagate on the Au-air interface and are instead scattered into the (±1, 0) and (0, ±1) Bloch modes allowed on this interface (Fig. 1(b)). Consequently, at the crystal boundary, where the symmetry of the lattice is broken, SPP beams couple to the smooth metal film in the *x* and *y* directions (Fig. 5(a,b)). This phenomenon is more visible in the case of a circular boundary, for which, the (1, ±1) SPP modes on the Au-glass interface impinge on the crystal boundary at normal incidence, thus minimising scattering by the nanostructure corners.

Whilst typically for complex beam-profile and non-diffracting SPP beam generation specially designed lattice geometries are used to provide the required phase relations, the discussion above illustrates how regular plasmonic crystals can be used for this purpose with a controlled illumination, via the generation of different SPP Bloch modes in the crystal. Moreover, as has been shown above, a focussed illumination allows for the excitation of multiple, spatially separated SPP beams at the same wavelength, propagating in multiple directions around a microscale SPPC.

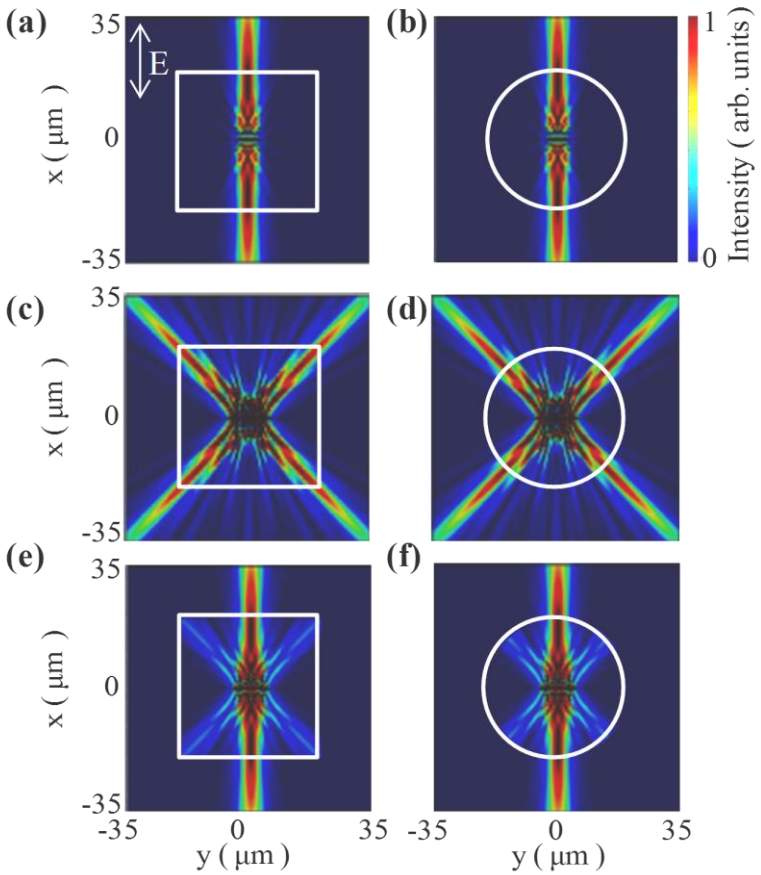

Fig.4: Numerically simulated SPP intensity on and near (a,c,e) the square (40 μm width) and (b,d,f) circular (40 μm diameter) SPPCs at the (a,b) Au-air, (c,d) Au-glass interfaces, and (e,f) the combination of the fields at both interfaces, considering a coupling coefficient of 0.1 within the crystal, corresponding to the SNOM measurements, when illuminated (1550 nm wavelength) at the centre with a collimated beam of a 10 μm diameter. The polarisation of the incident light is indicated in (a).

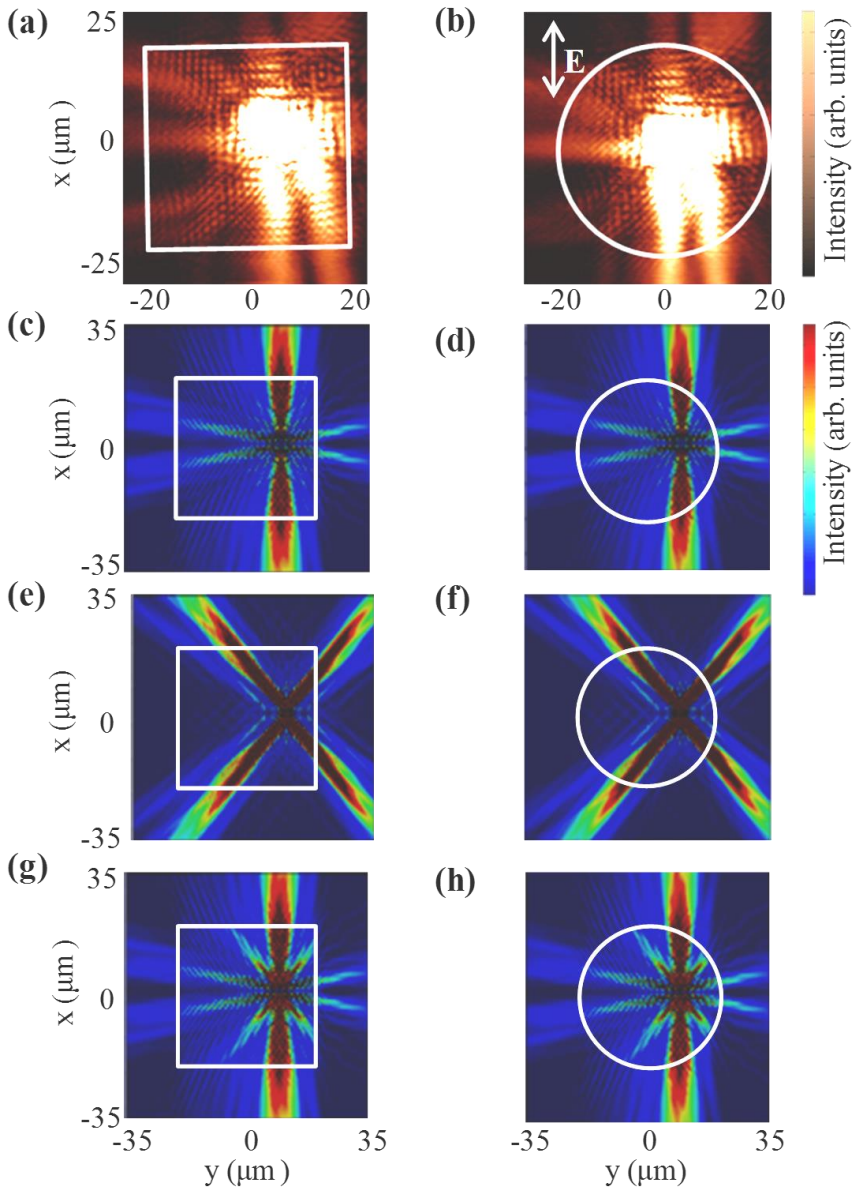

Fig.5: (a,b) Experimentally measured and (c-h) numerically simulated SPP intensity distributions on and near the square (40 μm width) and circular (40 μm diameter) SPPCs when off-centre illuminated with a focussed (N.A.=0.43) beam at 1550 nm wavelength. Numerically calculated SPP intensity distribution around the square and circular SPPC: at (c-d) the Au-air interface and (e-f) Au-glass interface. (g,h) Combination of the fields at both interfaces, considering a coupling coefficient of 0.1 within the crystal, corresponding to the SNOM measurements. The polarisation of the incident light is indicated in (b).

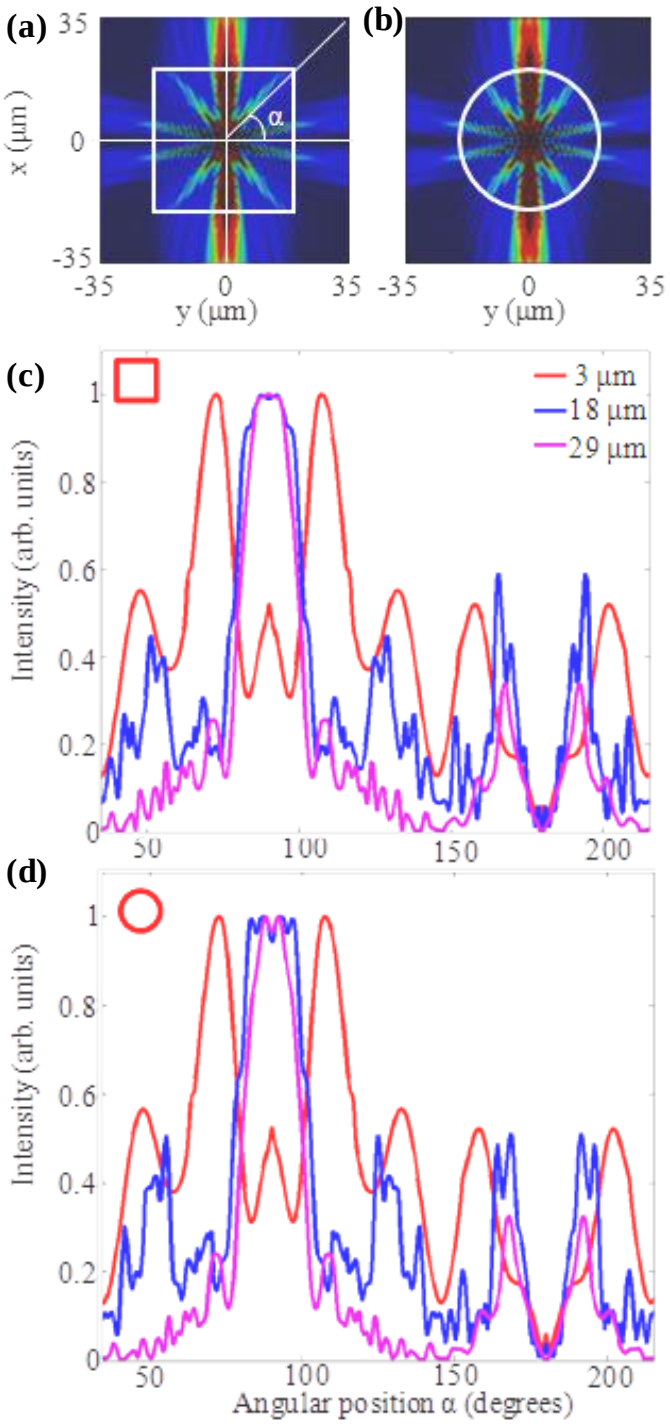

Fig.6: Numerically simulated SPP intensity distributions on and near the (a) square (40 μm width) and (b) circular (40 μm diameter) SPPCs when centrally illuminated with a focussed

(N.A.=0.43) beam for 1550 nm wavelength and detected in the near-field of the Au-air interface. Cross-section of the SPP intensity distributions at three distances around the (c) square and (d) circular SPPC centre.

4.3 Wavelength-dependent beam steering under focussed illumination

In order to understand the spectral dependence of the SPP coupling and to analyse its wavelength demultiplexing potential, the square crystal's response under focussed illumination was numerically studied in the wavelength range 1400-1700 nm (Fig. 7). Across the 1480-1590 nm spectral range, and in agreement with the behaviour observed above for a wavelength of 1550 nm, the (±1, 0) Bloch modes at the Au-air interface are preferentially coupled to. For a wavelength of 1400 nm, the range of incident wavevectors allows for the excitation of the (1, ±1) Bloch modes on the Au-air interface which are detected at angles $\alpha=36^o$ $\left(+n\frac{\pi}{2},\ n=0,1,2,3\right)$ around the SPPC centre, after propagation on the nanostructured area and refraction at the SPPC boundary. As the wavelength increases, however, the (1, ±1) Au-air Bloch modes can no longer be excited with the range of wavevectors present in the illumination and the SPP beams propagate solely along the (±1, 0) and (0, ±1) directions, for which propagation is still allowed on this interface.

The wavelength and polarisation dependent coupling efficiency of several Bloch modes can be useful for coarse wavelength demultiplexing applications. Fig. 7(a) shows the SPP spectrum around the SPPC as a function of the angular position 'α' (defined in Fig. 6(a)), measured within a 3 μm wide annular detector positioned at a distance of 32 μm from the SPPC centre. It can be seen that the wavelengths 1400 nm and 1540 nm can be spatially separated and detected with a -10 dB crosstalk, if detectors are placed at the angular positions $\alpha=36^o\pm4^o$ and $\alpha=72^o\pm4^o$ around the structure (Fig. 7(b)). Despite the low spectral resolution, the demultiplexing scheme presented here remains applicable to the integration and the interfacing of plasmonic functionalities with optical fibre technology, used ubiquitously for optical communications. The main advantage of this technology is the control of in-plane guided modes, a control not possible to achieve with traditional diffraction gratings, thus providing an alignment-free and integratable approach. In addition to the wavelength demultiplexing, transmission bands with less that 1dB variation in the detected power, can be obtained over large bandwidths (~100 nm) for specific direction propagations (e.g. $\alpha=45^o\pm4^o$, Fig. 7(b)).

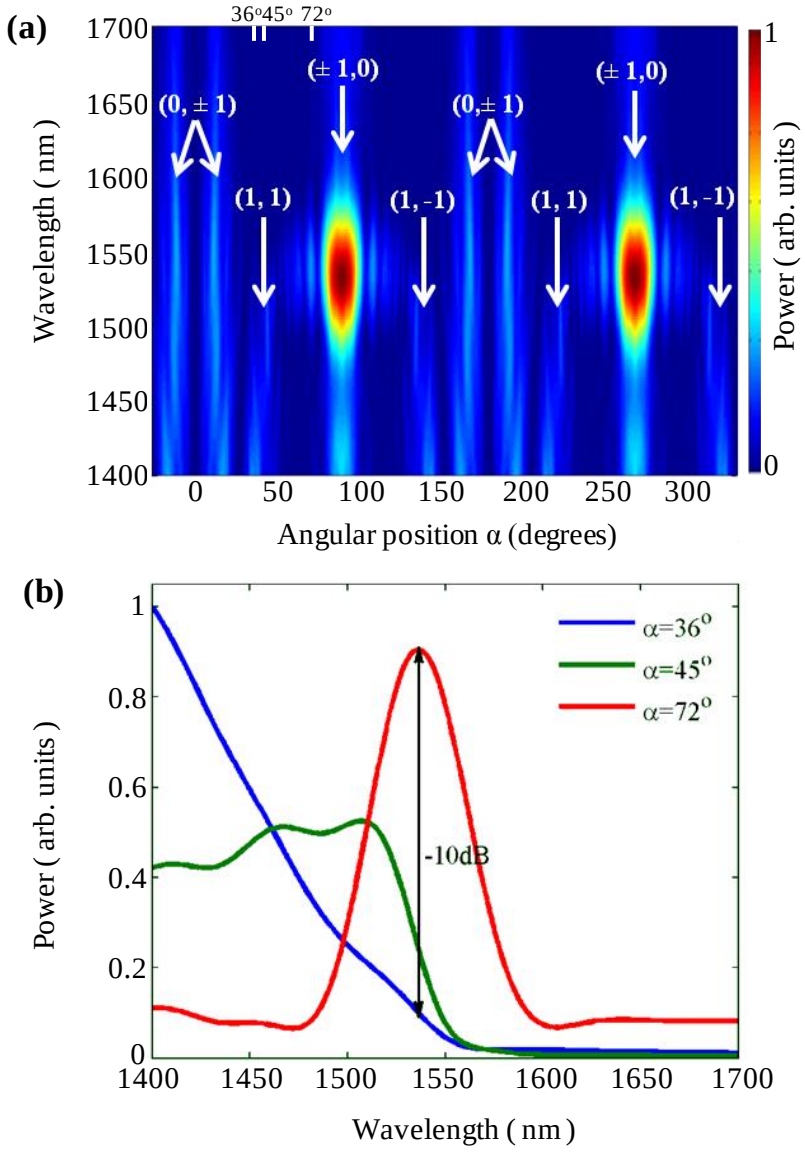

Fig. 7. (a) The angular dependence of the excited SPP modes around the crystal. (b) SPP spectra at several directions around the SPPC. The SPPC is illuminated in the centre with focussed (N.A.=0.43) light. The SPP power was calculated by integrating the SPP intensity over a 3 μm wide annular aperture positioned at a distance of 32 μm around the SPPC centre in the direction 'α'.

5. Conclusions

We have investigated the role of the boundary shape and the illumination conditions on the generation of plasmonic beams by finite size SPPCs in the telecommunication wavelength range around 1550 nm. Significant differences were identified in the excitation of broad SPP beams by plasmonic crystals with the same lattice but with different boundary shapes. The origin of these differences was explained by the relative phase-relations between the individual SPP scatterers at the boundary of the crystal, leading to complex interferences on the smooth metal film. In the case of the slowly varying boundary shapes considered in this work, the effect of the phase difference introduced by the various parts of the boundaries diminish for narrow beams due to the limited portion of the boundary that they interact with. One can however envisage more complex boundary shapes that would make full use of this phenomenon for plasmonic beams with reduced lateral sizes. Using focussed illumination, multiple narrow SPP beam excitation can be achieved at the same wavelength. The size, shape and lattice of SPPCs, as well as the illumination conditions, can be engineered to further manipulate the parameters of the generated SPP beams such as the beam width, focusing power, propagation direction and angular separation. The wavelength-dependent SPP coupling, which allows for a wavelength demultiplexing function and a flat transmission band is also described. This highlights a robustness and alignment-independent integration of applications combining SPP crystals with optical communication components.

Acknowledgements. This work was supported, in part, by EPSRC (UK) and the EC FP7 project PLAISIR. AZ and PB acknowledge support from the Royal Society and the Wolfson Foundation. Paulina Segovia thanks the support from CONACYT.

References

1. Barnes, W.L., A. Dereux, and T.W. Ebbesen, *Surface plasmon subwavelength optics.* Nature, 2003. **424**(6950): p. 824-830.
2. Brongersma, M.L. and V.M. Shalaev, *The Case for Plasmonics.* Science, 2010. **328**(5977): p. 440-441.
3. Zayats, A.V., I.I. Smolyaninov, and A.A. Maradudin, *Nano-optics of surface plasmon polaritons.* Physics Reports, 2005. **408**(3-4): p. 131-314.
4. Bozhevolnyi, S.I., et al., *Channel plasmon subwavelength waveguide components including interferometers and ring resonators.* Nature, 2006. **440**(7083): p. 508-511.
5. Dionne, J.A., et al., *Plasmon slot waveguides: Towards chip-scale propagation with subwavelength-scale localization.* Physical Review B, 2006. **73**(3):p.035407.
6. Fedyanin, D.Y., et al., *Surface Plasmon Polariton Amplification upon Electrical Injection in Highly Integrated Plasmonic Circuits.* Nano Letters, 2012. **12**(5): p. 2459-2463.
7. Holmgaard, T., et al., *Wavelength selection by dielectric-loaded plasmonic components.* Applied Physics Letters, 2009. **94**(5):p. 051111.
8. Krasavin, A.V., et al., *Optically-programmable nonlinear photonic component for dielectric-loaded plasmonic circuitry.* Optics Express, 2011. **19**(25): p. 25222-25229.
9. Krasavin, A.V. and A.V. Zayats, *Guiding light at the nanoscale: numerical optimization of ultrasubwavelength metallic wire plasmonic waveguides.* Optics Letters, 2011. **36**(16): p. 3127-3129.
10. Krasavin, A.V. and A.V. Zayats, *Photonic Signal Processing on Electronic Scales: Electro-Optical Field-Effect Nanoplasmonic Modulator.* Physical Review Letters, 2012. **109**(5): p.053901.

11. Papaioannou, S., et al., *Active plasmonics in WDM traffic switching applications.* Scientific Reports, 2012. **2**: p.652.
12. Randhawa, S., et al., *Experimental demonstration of dielectric-loaded plasmonic waveguide disk resonators at telecom wavelengths.* Applied Physics Letters, 2011. **98**(16): p.161102.
13. Zhao, C.L. and J.S. Zhang, *Plasmonic Demultiplexer and Guiding.* Acs Nano, 2010. **4**(11): p. 6433-6438.
14. Drezet, A., et al., *Plasmonic crystal demultiplexer and multiports.* Nano Letters, 2007. **7**(6): p. 1697-1700.
15. Sure, A., et al., *Fabrication and characterization of three-dimensional silicon tapers.* Optics Express, 2003. **11**(26): p. 3555-3561.
16. Bakir, B., *Low-Loss (< 1 dB) and Polarization-Insensitive Edge Fiber Couplers Fabricated on 200-mm Silicon-on-Insulator Wafers.* IEEE Photonics Technology Letters, 2010. **22**(11): p. 739-741.
17. Shoji, T., et al., *Low loss mode size converter from 0.3 μm square Si wire waveguides to singlemode fibres.* Electronics Letters, 2002. **38**(25): p. 1669-1670.
18. Almeida, V.R., R.R. Panepucci, and M. Lipson, *Nanotaper for compact mode conversion.* Optics Letters, 2003. **28**(15): p. 1302-1304.
19. Masanovic, G.Z., V.M. Passaro, and G.T. Reed, *Dual grating-assisted directional coupling between fibers and thin semiconductor waveguides.* IEEE Photonics Technology Letters, 2003. **15**(10): p. 1395-1397.
20. Taillaert, D., et al., *An out-of-plane grating coupler for efficient butt-coupling between compact planar waveguides and single-mode fibers.* IEEE Journal of Quantum Electronics, 2002. **38**(7): p. 949-955.
21. Taillaert, D., P. Bienstman, and R. Baets, *Compact efficient broadband grating coupler for silicon-on-insulator waveguides.* Optics Letters, 2004. **29**(23): p. 2749-2751.
22. Chen, X., C. Li, and H.K. Tsang, *Fabrication-tolerant waveguide chirped grating coupler for coupling to a perfectly vertical optical fiber.* IEEE Photonics Technology Letters, 2008. **20**(23): p. 1914-1916.
23. Sidiropoulos, T., M. P. Nielsen, T. R. Roschuk, A. V. Zayats, S. A. Maier, and R. Oulton, *A compact optical antenna coupler for silicon photonics characterized by third harmonic generation*. ACS Photonics, 2014. **1**(10): p. 912-916.
24. Bouillard, J.-S., et al., *Broadband and broadangle SPP antennas based on plasmonic crystals with linear chirp.* Scientific Reports, 2012. **2**: p. 829.
25. Krasavin, A.V. and A.V. Zayats, *Silicon-based plasmonic waveguides.* Optics Express, 2010. **18**(11): p. 11791-11799.
26. Salomon, L., et al., *Near-field distribution of optical transmission of periodic subwavelength holes in a metal film.* Physical Review Letters, 2001. **86**(6): p. 1110-1113.
27. Laux, E., et al., *Plasmonic photon sorters for spectral and polarimetric imaging.* Nature Photonics, 2008. **2**(3): p. 161-164.
28. Mikhailov, V., et al., *Dispersing light with surface plasmon polaritonic crystals.* Physical Review Letters, 2007. **99**(8): p.083901.
29. Elliott, J., et al., *Wavelength dependent birefringence of surface plasmon polaritonic crystals.* Physical Review B, 2004. **70**(23): p.233403.
30. Benetou, M.I., et al., *Four-level polarization discriminator based on a surface plasmon polaritonic crystal.* Applied Physics Letters, 2011. **98**(11): p. 111109.
31. Zayats, A.V., et al., *Polarization superprism effect in surface polaritonic crystals.* Applied Physics Letters, 2003. **82**(25): p. 4438-4440.

32. Baumberg, J.J., et al., *Angle-resolved surface-enhanced Raman scattering on metallic nanostructured plasmonic crystals.* Nano Letters, 2005. **5**(11): p. 2262-2267.
33. Stewart, M.E., et al., *Nanostructured plasmonic sensors.* Chemical Reviews, 2008. **108**(2): p. 494-521.
34. Benetou, M.I.e.a., *Microscale polarimeter based on a plasmonic crystal*, in *SPP5,2011, Busan*: p.135.
35. Bouillard, J.S., et al., *Optical transmission of periodic annular apertures in metal film on high-refractive index substrate: The role of the nanopillar shape.* Applied Physics Letters, 2010. **96**(20): p.201101.
36. Drezet, A., et al., *Opening the light extraction cone of high index substrates with plasmonic gratings: Light emitting diode applications.* Applied Physics Letters, 2009. **95**(2): p.021101.
37. Dickson, W., et al., *Electronically controlled surface plasmon dispersion and optical transmission through metallic hole arrays using liquid crystal.* Nano Letters, 2008. **8**(1): p. 281-286.
38. Le Guyader, L., et al., *Coherent control of surface plasmon polariton mediated optical transmission.* Journal of Physics D-Applied Physics, 2008. **41**(19):p.195102.
39. Wurtz, G.A., et al., *Controlling optical transmission through magneto-plasmonic crystals with an external magnetic field.* New Journal of Physics, 2008. **10**: p.105012.
40. Wurtz, G.A. and A.V. Zayats, *Nonlinear surface plasmon polaritonic crystals.* Laser & Photonics Reviews, 2008. **2**(3): p. 125-135.
41. Bouillard, J.S., et al., *Low-temperature plasmonics of metallic nanostructures.* Nano Letters, 2012. **12**(3): p. 1561-5.
42. Bouillard, J.-S., et al., *Shaping plasmon beams via the controlled illumination of finite-size plasmonic crystals.* Scientific Reports, 2014. **4**:p.7234.
43. Stein, B., et al., *Surface Plasmon Mode Steering and Negative Refraction.* Physical Review Letters, 2010. **105**(26):p.266804.
44. Bouillard, J.S., et al., *Hyperspectral imaging with scanning near-field optical microscopy: applications in plasmonics.* Optics Express, 2010. **18**(16): p. 16513-16519.
45. Bouillard, J.-S.G., et al., *Near-Field Hyperspectral Optical Imaging.* Chemical Physics and Physical Chemistry, 2014. **15**(4): p. 619-629.
46. Coello, V. and S.I. Bozhevolnyi, *Surface plasmon polariton excitation and manipulation by nanoparticle arrays.* Optics Communications, 2009. **282**(14): p. 3032-3036.
47. Smolyaninov, I.I., C.C. Davis, and A.V. Zayats, *Image formation in surface plasmon polariton mirrors: applications in high-resolution optical microscopy.* New Journal of Physics, 2005. **7**:p.175.
48. Sondergaard, T. and S.I. Bozhevolnyi, *Vectorial model for multiple scattering by surface nanoparticles via surface polariton-to-polariton interactions.* Physical Review B, 2003. **67**(16): p.165405.
49. Segovia, P. and V. Coello, *Elastic Surface Plasmon Polariton Scattering: Near- and Far-Field Interactions.* Nano, 2012. **7**(1): p.1150003.
50. Søndergaard, T. and S. Bozhevolnyi, *Surface plasmon polariton scattering by a small particle placed near a metal surface: An analytical study.* Physical Review B, 2004. **69**(4): p. 045422.
51. Cho, S.B., et al., *Vector wave analysis for nonnormal incident rays in epimicroscopic refractive index profile measurements.* Applied Optics, 2008. **47**(2): p. 157-163.

52. Smolyaninov, I. I., C. C. Davis, and A. V. Zayats, *Image formation in surface plasmon polariton mirrors: applications to high-resolution optical microscopy*. New Journal of Physics, 2005. **7**: 175.
53. Evlyukhin, A., et al., *Focusing and directing of surface plasmon polaritons by curved chains of nanoparticles.* Optics Express, 2007. **15**(25): p. 16667-16680.
54. Garcia-Ortiz, C.E., et al., *Generation of diffraction-free plasmonic beams with one-dimensional Bessel profiles.* Optics Letters, 2013. **38**(6): p. 905-907.
55. Li, L., et al., *Collimated plasmon beam: nondiffracting versus linearly focused.* Physical Review Letters, 2013. **110**(4): p. 046807.
56. Lin, J., et al., *Cosine-Gauss plasmon beam: a localized long-range nondiffracting surface wave.* Physical Review Letters, 2012. **109**(9): p. 093904.
57. Liu, Z., et al., *Focusing surface plasmons with a plasmonic lens.* Nano Letters, 2005. **5**(9): p. 1726-1729.
58. Minovich, A., et al., *Generation and near-field imaging of Airy surface plasmons.* Physical Review Letters, 2011. **107**(11): p. 116802.
59. Altewischer, E., et al., *Resonant Bragg scatter of surface plasmons on nanohole arrays.* New Journal of Physics, 2006. **8**:p.1-14